AGU PUBLICATIONS

JGR

Journal of Geophysical Research: Space Physics

RESEARCH ARTICLE

10.1002/2016JA023712

Key Points:
- We estimate detailed parameters of the Ceres bow shock inferred by energetic electron beams observed by Dawn
- We use a single-fluid MHD model and a multifluid plasma model to show how interaction conditions affect the shock formation
- Occurrence of a shock requires a gas production rate above 1.8 kg/s at Ceres

Correspondence to:
Y.-D. Jia,
yingdong@igpp.ucla.edu

Citation:
Jia, Y.-D., M. N. Villarreal, and C. T. Russell (2017), Possible Ceres bow shock surfaces based on fluid models, *J. Geophys. Res. Space Physics*, *122*, 4976–4987, doi:10.1002/2016JA023712.

Received 18 NOV 2016
Accepted 12 APR 2017
Accepted article online 18 APR 2017
Published online 3 MAY 2017

Possible Ceres bow shock surfaces based on fluid models

Y.-D. Jia[1], M. N. Villarreal[1], and C. T. Russell[1]

[1]IGPP and EPSS, University of California, Los Angeles, California, USA

Abstract The hot electron beams that Dawn detected at Ceres can be explained by fast-Fermi acceleration at a temporary bow shock. A shock forms when the solar wind encounters a temporary atmosphere, similar to a cometary coma. We use a magnetohydrodynamic model to quantitatively reproduce the 3-D shock surface at Ceres and deduce the atmosphere characteristics that are required to create such a shock. Our most simple model requires about 1.8 kg/s, or 6×10^{25}/s water vapor production rate to form such a shock. Such an estimate relies on characteristics of the solar wind-Ceres interaction. We present several case studies to show how these conditions affect our estimate. In addition, we contrast these cases with the smaller and narrower shock caused by a subsurface induction. Our multifluid model reveals the asymmetry introduced by the large gyroradius of the heavy pickup ions and further constrains the IMF direction during the events.

Plain Language Summary This study estimates detailed parameters of the Ceres bow shock inferred by energetic electron beams arriving at Dawn. We present results using a single-fluid MHD model and a multifluid MHD model to show how the interaction conditions affect the shock formation. While observation favors global exosphere with no significant body induction, we found that a shock requires a gas production rate above 1.8 kg/s at Ceres.

1. Introduction

In a slightly eccentric orbit at 2.6–3 AU from the Sun, the dwarf planet Ceres has a radius about 13 times smaller than that of the Earth, and about 4 times smaller than that of the Moon. Such a small body at this distance from the Sun cannot retain a permanent atmosphere, as also confirmed by terrestrial telescopes over the past three decades. The first suggestion of a transient atmosphere was by *A'Hearn and Feldman* [1992], who saw OH emissions above the Cerean north pole on one of two observing sessions. More recently, *Küppers et al.* [2014] reported H_2O absorption lines obtained by the Herschel Space Observatory (HSO). They interpreted this as indicating a short-lived exosphere around Ceres, escaping at about 6 kg/s flux, possibly arising from a small area where ice sublimates near the surface.

Dawn's payload does not include instrument designed to measure the plasma density and magnetic field. However, as Dawn approached Ceres, electron beams of some tens of keV were detected by its Gamma Ray and Neutron Detector (GRaND) [*Prettyman et al.*, 2011], arriving from the direction of Ceres, over a 7 day period between 19 and 26 June 2015 [*Russell et al.*, 2016]. A very plausible source of such electrons are foreshock electrons [*Wu*, 1984], accelerated from the solar wind at a standing bow shock surface in front of Ceres. Dawn remained in this 10 Ceres radii (R_c) Survey orbit for about a month before descending to lower orbits, namely, the high-altitude mapping orbit (HAMO) at about 4 R_c and the low-altitude mapping orbit (LAMO) at 1.8 R_c. At the completion of our work, Dawn has not returned to the Survey orbit. No additional electron bursts have been observed since June 2015, implying that the shock was only temporary, lasting for about a week. There are two physically possible ways to form temporary shocks at Ceres: a transient exosphere or an induced magnetic field compressed by the solar wind.

The arrival of a solar proton event in conjunction with the onset of the electron acceleration suggests that the solar event activated the surface of Ceres at the time of the GRaND detections. Particles may have been sputtered by solar energetic protons creating a temporary exosphere that then decayed over the following week [*Villarreal et al.*, 2017]. This timescale would be expected for a temporary Ceres atmosphere [*Formisano et al.*, 2016]. *Russell et al.* [2016] used a magnetohydrodynamic (MHD) model to illustrate the probability that the interplanetary magnetic field (IMF) that also connected to Dawn during the electron events was tangent to the

Ceres's standing shock surface. In this paper, we provide more details of that MHD model, and determine the strength of an atmosphere necessary to create such a shock as well as the dimension of the shock in response to this inferred atmosphere. Section 2 shows the two models that are used in this paper, section 3 shows the results of the two models with a collection of case studies under different assumptions, and section 4 concludes the paper.

2. Model Description

To expand upon our previous estimate [*Russell et al.*, 2016], we show more cases of the single-fluid MHD simulation to calculate the expected shock position for different solar wind and atmospheric conditions. The standard MHD model that we used for the first five cases assumes an ion gyroradius smaller than the grid size, while the actual ion gyroradius is larger than Ceres. Thus, the MHD result is useful in estimating the shock distance and the size of the atmosphere while not necessarily replicating downstream conditions. Next, we provide a multifluid plasma simulation to assess the limitations of the single-fluid code. We define the control equations of both models in this section.

2.1. Single-Fluid Ideal MHD Equations

This is the classical MHD equation set found in textbooks, which has been previously applied to Saturn's moons [*Jia et al.*, 2010]. The state variables calculated in this set of equations are the plasma mass density ρ, velocity vector $\mathbf{u}$, thermal pressure scalar $p = nkT$, and magnetic field vector $\mathbf{B}$. Among them, ρ is the product of ion number density n with ion mass m. The thermal pressure of the electrons is assumed to be equal to the ion thermal pressure: $p_e = p_i = p/2$. The current density $\mathbf{J}$ is calculated with Ampere's law: $\mathbf{J} = \nabla \times \mathbf{B}/\mu_0$.

The magnetic field is convected by the plasma: $\partial \mathbf{B}/\partial t = (\nabla \times \mathbf{u} \times \mathbf{B})$. Our governing equations require that the mass density ρ, momentum density $\rho\mathbf{u}$, and thermal energy density represented by thermal pressure p is conserved during this process, respectively:

$$\frac{\partial \rho}{\partial t} + \nabla \cdot (\rho \mathbf{u}) = Q_\rho \tag{1}$$

$$\frac{\partial (\rho \mathbf{u})}{\partial t} + \nabla \cdot (\rho \mathbf{u}\mathbf{u}) = \rho \mathbf{g} - \nabla p + \mathbf{J} \times \mathbf{B} + \mathbf{Q}_M \tag{2}$$

$$\frac{\partial p}{\partial t} + \nabla \cdot (p\mathbf{u}) = -(\gamma - 1)\, p\, (\nabla \cdot \mathbf{u}) + Q_p, \tag{3}$$

where $\gamma = 5/3$ is the adiabatic constant, and source term Q includes effects of ions added to and removed from the calculation domain via impact ionization $\mathrm{IN} = mn_n f_i$, and charge exchange $\mathrm{CX} = mn_n n k_{\mathrm{in}}$ [*Jia et al.*, 2010]:

$$Q_\rho = \mathrm{IN} \tag{4}$$

$$Q_M = (\mathrm{IN} + \mathrm{CX})\mathbf{u}_n - \mathrm{CX}\,\mathbf{u} \tag{5}$$

$$Q_p = \frac{\gamma - 1}{2}(\mathrm{IN} + \mathrm{CX})(\mathbf{u}_n - \mathbf{u})^2 + \frac{k}{m}(2\mathrm{IN}\, T_n + \mathrm{CX}(T_n - T_i)), \tag{6}$$

where $\mathbf{u}_n$ is the neutral velocity, n_n is the neutral density, f_i is the combined rate of photoionization and impact ionizations, k_{in} is the ion-neutral charge exchange rate, and k is the Boltzmann constant. The $2\mathrm{IN}\, T_n$ term in the pressure equation calculates contributions from neutral temperature to both ion temperature and electron temperature due to photoionization and impact ionization.

2.2. Multifluid Plasma Equations

In contrast to the single-fluid MHD model, the multifluid model treats the solar wind protons, water group ions, and the electrons as three coupled fluids. Such a model has recently been applied to the lunar wake in agreement with large-scale hybrid simulation results modeling solar wind-Moon interactions with proton gyroradius about 0.6 Moon radii [*Zhang et al.*, 2016]. Here the electron fluid is assumed massless, and its density is calculated assuming quasi-neutrality: $n_e = \Sigma_s n_s Z_s$, where the subscript s runs through all massive fluids, and Z is the number of proton charges that each particle of the fluid carries. The electron velocity is calculated

Table 1. Solar Wind Parameters Extrapolated From Averaged ACE Measurement During the Week of 17 to 24 June[a]

Variables	Values
Solar wind density n_{sw}	1.3/cm^3
Solar wind velocity u_{sw}	500 km/s
Solar wind temperature T_{sw}	2×10^5 K
IMF $(B_x, B_y, B_z)_{sw}$	(−1.2, 0.88, −0.45) nT
Plasma β	2

[a]Earth is about 30° from the upstream of Ceres in June 2015.

by the definition of electric current: $\mathbf{u}_e = \Sigma_s n_s Z_s \mathbf{u}_s / n_e - \mathbf{J}/en_e$, where e is the proton charge. The temperature of the electrons is assumed to be the average of the temperature of massive ion species: $T_e = \frac{\Sigma_s n_s Z_s T_s}{n_e}$, to be consistent with the single-fluid model.

At 3 AU, the gyroradius of electrons is around 1 km, which can be safely neglected when discussing structures of hundreds of kilometers and larger [*Jia et al.*, 2014]. Thus, the magnetic field is carried by the electron fluid: $\partial \mathbf{B}/\partial t = \nabla \times (\mathbf{u_e} \times \mathbf{B})$.

The same conservation laws applied to the single-fluid equations (1)–(3) are now applied to each of the two massive fluids:

$$\frac{\partial \rho_s}{\partial t} + \nabla \cdot \left(\rho_s \mathbf{u}_s\right) = Q_{\rho s} \tag{7}$$

$$\frac{\partial \left(\rho_s \mathbf{u}_s\right)}{\partial t} + \nabla \cdot \left(\rho_s \mathbf{u}_s \mathbf{u}_s\right) = \rho_s \mathbf{g} - \nabla p_s - \frac{n_s}{n_e} Z_s \nabla p_e + n_s Z_s e \left(\mathbf{u}_s - \mathbf{u}_e\right) \times \mathbf{B} + \mathbf{Q}_{Ms} \tag{8}$$

$$\frac{\partial p_s}{\partial t} + \nabla \cdot \left(p_s \mathbf{u}_s\right) = -\left(\gamma - 1\right) p_s \left(\nabla \cdot \mathbf{u}_s\right) + Q_p s. \tag{9}$$

We define the mass addition and loss rates as follows: $S_s = \sum_{s'=\text{neutrals}} m_s n_{s'} (f_{ss'} + \sum_{t=\text{ions}} k_{s't-st'} n_t)$, $L_s = \sum_{t'=\text{neutrals},t=\text{ions}} m_s n_{t'} n_s k_{t's-ts'}$, where $f_{ss'}$ is the rate of photo and impact ionizations from neutral species s' into ion species s, $k_{s't-st'}$ is the ion-neutral charge exchange rate between neutral species s' and ion species t, producing ion species s and neutral species t'. Thus, the source terms in the conservation equations are

$$Q_{\rho s} = S_s - L_s \tag{10}$$

$$Q_{Ms} = S_s \mathbf{u}_n - L_s \mathbf{u}_s \tag{11}$$

$$Q_{ps} = \frac{\gamma - 1}{2} S_s (\mathbf{u}_n - \mathbf{u}_s)^2 + \frac{k}{m_s} (S_s T_n - L_s T_s), \tag{12}$$

where the neutral velocity $\mathbf{u}_n$ is assumed to be the same for all neutral species. We also neglect the temperature difference of all neutral species.

2.3. Numerical Model Setup

In June 2015, Ceres was 2.8 AU from the Sun, and less than 30° ahead of the Earth in its orbit, close enough to extrapolate and estimate the solar wind conditions at Ceres. It takes about 6 days for a 500 km/s solar wind to travel 1.8 AU. The Advanced Composition Explorer (ACE) and Wind measurements (http://cdaweb.gsfc.nasa.gov/) between 13 and 19 June are averaged to extrapolate the solar wind values at 2.8 AU [*Smith and Wolfe*, 1979]. Solar wind conditions shown in Table 1 are assumed to be steady during the time of the event simulation.

Our simulations are based on a Cartesian grid, measured by the Ceres Solar Orbital (CSO) coordinate system, where Ceres centers at the origin, the x vector points from the Sun to Ceres, the z axis is parallel to the Ceres orbital axis, and the y axis completes the right-handed system. In most cases, the finest grid resolution is 1/12 R_c around the shock and Ceres. An exception is applied to case 2, where we found from our convergence test [*Jia et al.*, 2007] that the weaker atmosphere requires a higher resolution of 1/24 R_c, which is used only for case 2. The simulation domain is a $80 \times 40 \times 40$ R_c rectangular box. The outer boundaries of this domain use solar wind inflow on the $x < 0$ side, and outflow on the five other sides.

The inner boundary is located on the Ceres surface. Two types of inner boundary conditions are used: an exospheric boundary and an inductive boundary. The exospheric boundary [*Jia et al.*, 2010] is examined first. On reaching the surface of Ceres, the solar wind flow is absorbed. The density for water ions released from the

Table 2. List of All Simulation Cases

Case Number	Fluids	Inner BC	Gas Flux Q	Solar Wind
Case 1	Single	Exosphere	9 kg	Solar wind
Case 2	Single	Exosphere	1.8 kg	Solar wind
Case 3s	Single	Sunward plume	4.5 kg	Solar wind
Case 3t	Single	Tailward plume	4.5 kg	Solar wind
Case 3l	Single	Sunward plume	0.9 kg	Solar wind
Case 4	Single	Exosphere	9 kg	Double density
Case 5	Single	Induction	0 kg	Solar wind
Case 6p	4	Exosphere	9 kg	Solar wind
Case 6n	4	Exosphere	9 kg	Negative IMF

surface is set to a minimum value, which is 10^{-6} times the solar wind density, its temperature equals the surface value, and its velocity is zero on the surface. For this condition, the magnetic field has no gradient across Ceres's surface. For the second condition, the inductive boundary assumes perfect induction at the Ceres surface, to simulate the effect of a possible underground salt-rich, electrically conducting, muddy layer that repels the incoming IMF [*Castillo-Rogez*, 2011]. For this condition, the radial vector components of both the plasma flow and the magnetic field are zero at the Cerean surface. This condition is applied to our simulation case 5, as summarized in Table 2.

The gas around Ceres is modeled as a spherically symmetric water vapor exosphere with a constant flux of $Q = 9$ kg/s, or 3×10^{26}/s, so the neutral density at distance r from the origin is $N_n = Q/4\pi u_n r^2$. This is equivalent to a number density $N_0 = 3 \times 10^{11}/\mathrm{cm}^3$ uniformly distributed on the surface. For comparison, this surface density is several times smaller than the HSO value [*Küppers et al.*, 2014], which was assumed to be concentrated in a localized region. The neutral speed $u_n = 360$ m/s directed radially outward is consistent with a surface temperature of 170 K. The neutral temperature T_n is also set as this constant. The surface rotation speed is 90 m/s at the equator, which is neglected in this model.

The chemical reaction rates assume water group neutrals in the exosphere, and the solar radiation intensity at 2.8 AU: the impact-ionization rate is $j_v = 10^{-7}$/s for both hydrogen and water group neutrals. The charge exchange rate averages to $k_{\mathrm{in}} = 2 \times 10^{-15}$ m^3/s for all reactions. A more accurate model may include charge exchange rates for individual reactions separately [*Shou et al.*, 2015], but our estimation in section 4 shows that charge exchange is not as important as photoionization and impact ionization combined, so an averaged number is used.

3. Case Studies

To reproduce the shock that accelerated the solar wind electrons, we seek a steady state solution using constant solar wind conditions, as listed in Table 1 and then note in Table 2 if the value is different. We start with a simplified case, to estimate the lower limit of the outgassing rate, and then reevaluate the rate for different conditions.

3.1. Case 1: Solar Wind-Exosphere Interaction in the Single-Fluid Model

In comparison with our previous work, we first use parameters similar to the case shown by *Russell et al.* [2016], with an IMF vector that connects the shock surface and the detection locations. The outgassing rate is set to 9 kg/s, or 3×10^{26}/s, which is an order of magnitude lower than the value used by *Russell et al.* [2016], to be compatible with the Hubble Space Telescope (HST) detection limit of 4×10^{26}/s in the far ultraviolet (FUV) wavelength by *Roth et al.* [2016].

The case 1 results are shown in Figures 1 and 2. In our 3-D plot, the axis in Figure 1 is rotated to the optimum angle to display the slightly bent magnetic field lines at the shock surface. A straight line (not shown) passing the same pair of displayed starting-ending points of any of these field lines would have penetrated into the shock surface. An interactive 3-D view of the case 1 shock can be found at http://redcat.igpp.ucla.edu/yingdong/RRR/Ceres/ShkCeC1.xhtml. This upstream compression is due to local pickup from the exosphere of Ceres. The approximate radial distance from Ceres to the tangential points are between 5 and 10 R_c, as marked in Figure 2. The subsolar distance of the shock is about 1.3 R_c.

The field lines in Figures 1 and 2 are examples of one possible IMF direction. It is also possible, although different from the Parker spiral, that the IMF touches the shock surface on the $+y$ side. However, the tangential points will be far from Ceres, with their x coordinate estimated to exceed 20 R_c, where the shock is supposed to be very weak. Therefore, we believe that it is unlikely that the IMF touched the shock surface on the $+y$ side.

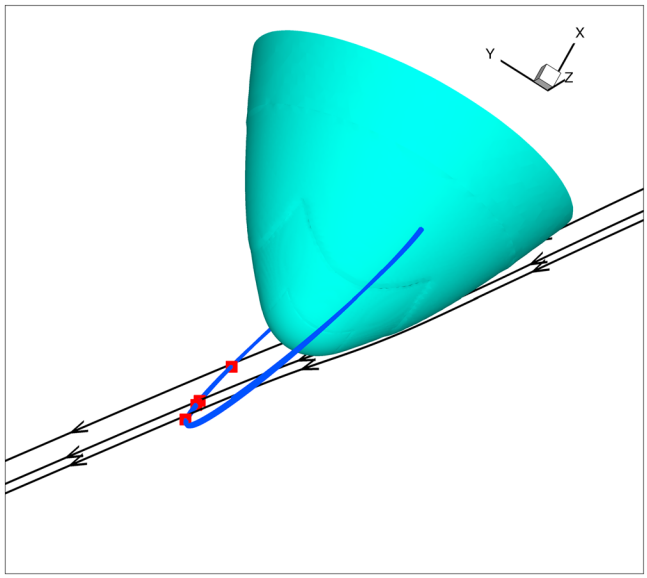

Figure 1. Case 1, Ceres shock marked by the cyan isosurface of density $\rho = 2$ amu/cm^3 in 3-D. The blue circle is the trajectory (projected into one thick blue line). The locations of beam detection are marked by red squares. The black lines with arrows are 3-D magnetic field lines.

As shown in Figure 2, the shock surface is close to being axially symmetric. Close to the tangential points of the field lines, the flaring angle of the shock surface is about arctan(2/3), or 35°, very close to the IMF cone angle of about 39°, forcing a very rapid movement of the compression region on the shock surface, relative to the incoming IMF. This result is consistent with the findings of [*Russell et al.*, 2016], that a temporary exosphere is responsible for these keV electrons.

3.2. Case 2: Constraint on the Gas Escape Rate

Previous observations put no constraint on the minimum outgassing rate needed to produce a weak shock, similar to that is expected at the end of the electron burst event, so it is necessary to use our model to determine the minimum atmospheric outgassing rate that could produce such a weak shock.

Figure 3 shows the result for case 2, which has an outgassing rate of 6×10^{25}/s. This rate is 5 times lower than the value used in case 1. The shape of the shock remains the same, but the shock is almost touching the Ceres surface, and the density gradient in the color contour is weaker than that of case 1. A test case (not shown) with a 3×10^{25}/s outgassing rate did not produce an identifiable shock, resulting only in a wake structure comparable to that of comet 67P/Churyumov–Gerasimenko at a heliocentric distance of 3.25 AU [*Hansen et al.*, 2007].

From the results above, we find that the lower limit of the atmosphere intensity necessary to sustain a bow shock to provide the electron acceleration is 6×10^{25}/s. This is consistent with the loss rate dropping from 3×10^{26}/s to 6×10^{25}/s in the course of 7 days. The cases below examine how our assumptions may have affected the accuracy of this lower limit.

3.3. Case 3: Effect of the Exospheric Shape

The HSO observations appear to favor an asymmetric exosphere originating from local sources, either by comet-like sublimation or by Enceladus-like cryovolcanism [*Küppers et al.*, 2014]. In case 3, we launch three

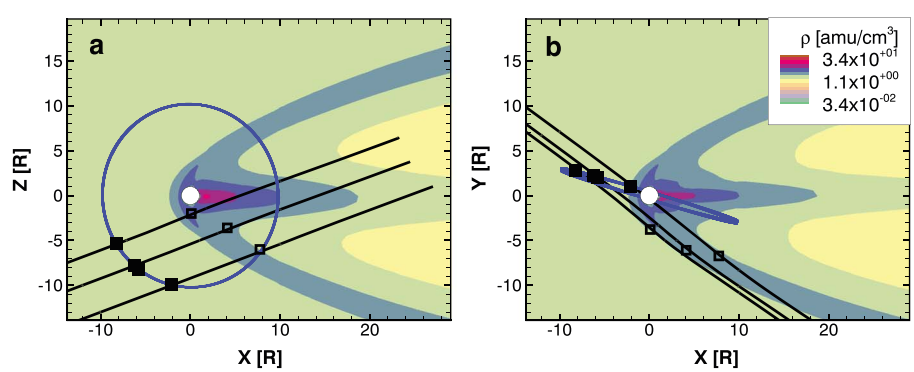

Figure 2. Ceres shock shown in 2-D slices from the case 1 result. The same field lines shown in Figure 1 are also projected into the two planes. The blue circle represents the trajectory of DAWN between 18 and 27 June 2015. The solid squares are the location of detection, while the hollow squares are the approximate locations where the field lines are closest to the shock surface. The contour levels in left and right panels are the same.

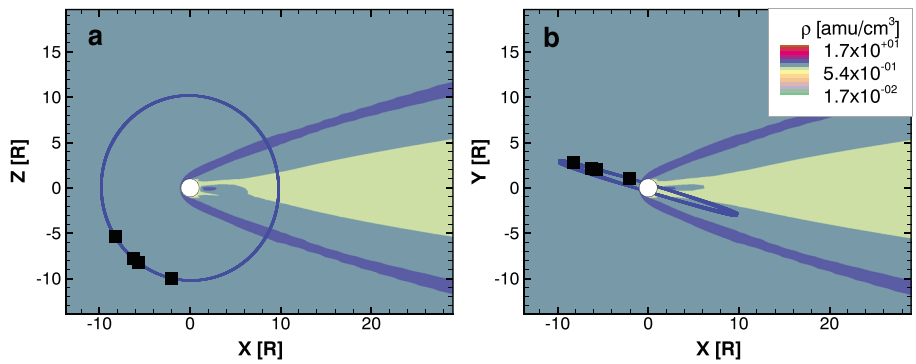

Figure 3. Case 2, Ceres shock with a weak exosphere, shown in 2-D slices. The blue circle and solid squares represent DAWN location, following the same legend as used in Figure 2.

model runs to study the shape of the shock created by a plume pointing in two different directions. The difference in these three cases are also detailed in Table 2. There are several possible surface locations of such a water source, and the gas source on the surface may corotate with Ceres. It takes about 20 min for a newly released water molecule to travel 1 Ceres radii, which is farther than the subsolar standoff distance of the bow shock in case 1 result. In 20 min, the source will only move 10°, at the 9.1 h spin period of Ceres. Hence, we neglect rotation and use a steady state plume in a fixed arbitrary location to demonstrate the effect of an asymmetric exosphere. In all three runs, the spherically symmetric atmosphere used in earlier cases is replaced by a plume with a 20° cone angle, inside the *x*-*z* plane, 60° from the $-z$ axis. The gas is concentrated in a cone, raising the peak surface number density by 2 orders of magnitude.

Our first of these runs, case 3s, applies a total gas flux of 1.5×10^{26}/s (4.5 kg/s) in the plume, which results in a peak surface density of $N_s = 1 \times 10^{14}/\mathrm{m}^3$. The plume points 60° sunward of the $-z$ axis. As shown in Figures 4a and 4b, such a concentrated gas plume causes a stronger shock, encompassing the Dawn's orbit around Ceres. The accelerated electrons cannot be seen inside the shock, so the total escape rate should be lower than this value, if it is concentrated in a plume toward the Sun.

Figures 4c and 4d show the results for case 3t, in which, the plume is pointing 60° from the $-z$ axis, away from the Sun with the same gas flux as case 3s. This bow shock is stronger than the case 1 shock due to an increased gas density, but the location is comparable. The shock is wider in the *x*-*z* plane and narrower in the *x*-*y* plane, requiring the IMF to be mainly B_x and B_z, in order for the IMF that connects Dawn and the shock to be tangential to the shock surface.

Comparing Figures 4b and 4d to Figure 2, the case 3 shocks are comparable to the case 1 shock when the plume is pointing sunward (case 3s) but becomes narrower when the plume is pointing away from the Sun (case 3t). Our result indicates that the Kuppers exosphere (6 kg/s flux tailward *Küppers et al.* [2014]) is sufficient to create a shock, but the tail-pointing plume may result in a narrow shock surface in the plane quasi-parallel to Dawn's orbital plane around Ceres.

To estimate the lower limit for the outgassing rate of a plume, we run case 3l, a plume pointing in the same direction as case 3s did, with a flux 10 times lower. The result is shown in Figures 4e and 4f. The plume is still strong enough to sustain a shock. Thus, if the gas is concentrated in a plume, the lower limit for the gas production rate can be below 1.5×10^{25}/s, less than that needed in the global exosphere case. Comparing Figures 3 and 4, we expect the lower limit for the plume case to be a few times smaller than this value. The 9.1 h spin period of Ceres may rotate the shock shape between the extremes represented by cases 3s and 3t. We would again expect modulation of the accelerated electrons at Ceres rotation period during the 7 days of observation.

3.4. Case 4: Effect of the Solar Wind

For cases 1–3, we have chosen our solar wind conditions by extrapolating averaged Earth measurements during the 7 day period. The ACE data show a small change in velocity, but significant changes in density, and the magnetic field vector. Therefore, the solar wind we used could be different than the actual conditions by some factor at the moment of detection. Case 4, shown in Figure 5, uses a solar wind condition with a density twice that of case 1, as shown in Table 2. The shock retains the same shape as in case 1, but is compressed

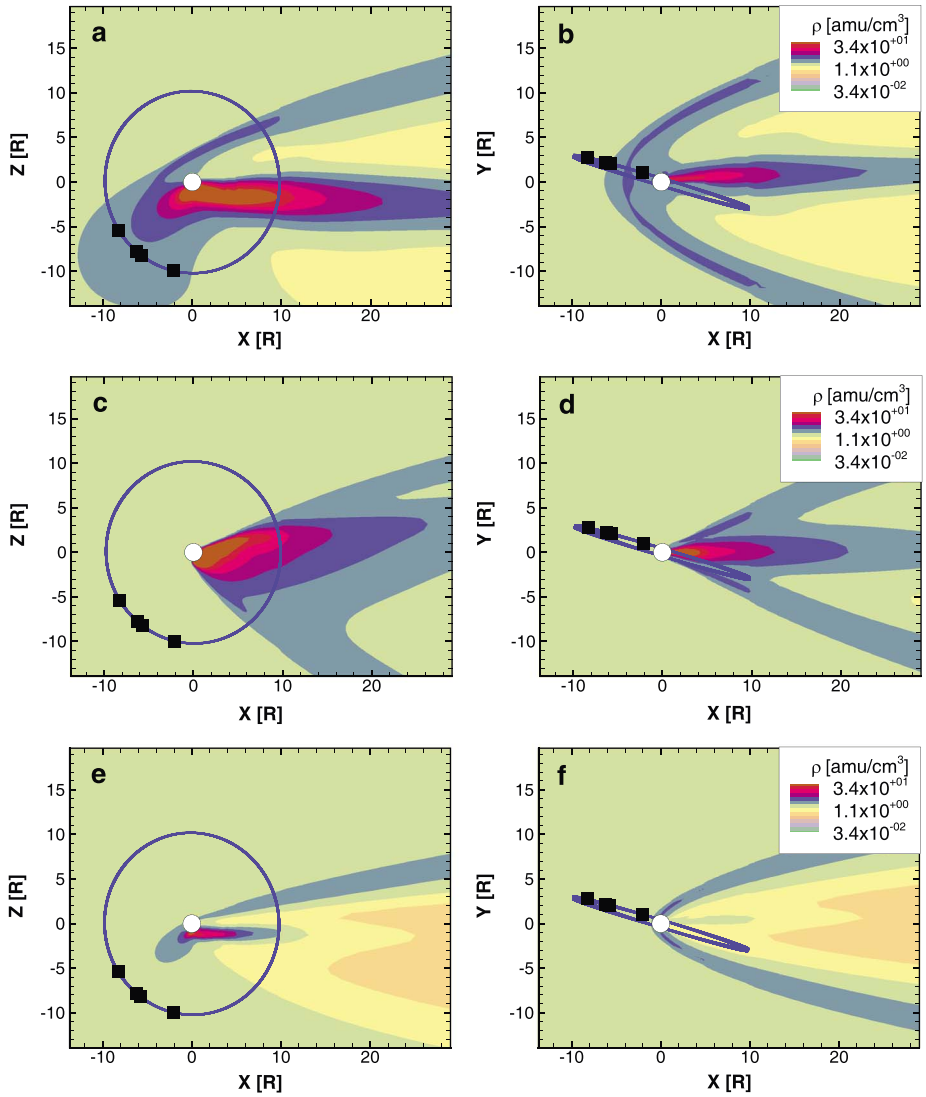

Figure 4. Case 3, Ceres shock with all outgassing concentrated in a plume: (a, b) antisunward plume (case 3s), (c, d) wake plume (case 3t), and (e, f) antisunward weak plume (case 3l).

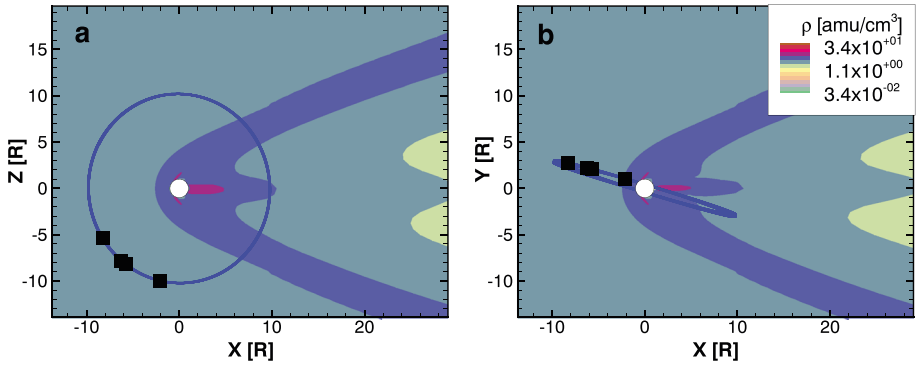

Figure 5. Case 4, Ceres shock in a solar wind density twice as much as that of case 1.

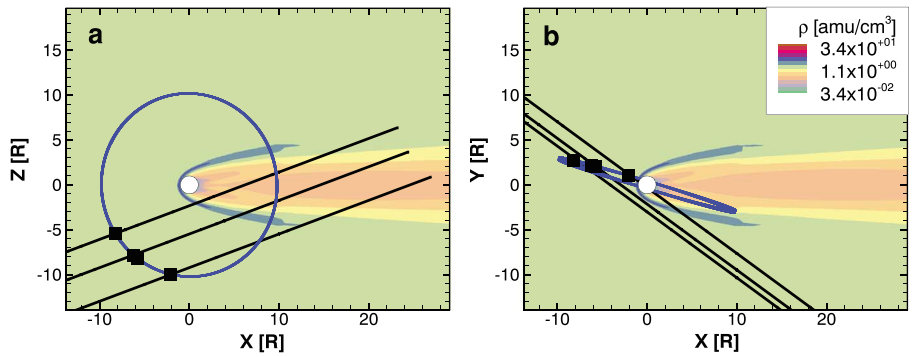

Figure 6. Ceres shock shown in 2-D slices from case 5 model result. The same field lines are projected from 3-D into the two planes. Ceres trajectory and locations of detection are shown in the same fashion as those in Figure 2.

closer to the Cerean surface. This can be understood by the doubled solar wind dynamic pressure compressing the induced mini magnetosphere supported by pickup ions. Since stronger solar wind pressure decreases the shock size, we believe that the lower limit of the gas production rate should be higher with a stronger solar wind. An increased solar wind velocity would have the same effect.

On the other hand, although the IMF direction is constrained by the spacecraft location and the shock surface, the intensity of the IMF changed during the week-long period. For a stronger IMF intensity, the induced magnetic field in the ionized cloud around Ceres would be stronger. Consequently, the subsolar point of the shock would be farther out. Hence, we also simulated in case 4 using an IMF twice as strong as that used for case 1. Doing so moved the subsolar point of the shock out to 1.5 R_c (not plotted).

3.5. Case 5: Solar Wind-Conductive Ocean Interaction

Models have shown that Ceres may have a conductive muddy layer with a high concentration of salts [*Castillo-Rogez*, 2011]. Therefore, a bow shock may form in the solar wind in response to an ICME, even without any pickup from the Cerean exosphere. Although *Russell et al.* [2016] found it unlikely that a week-long shock could be sustained solely by ocean induction, here we show the shock shape for such cases. In case 5, we model the solar wind-Ceres interaction with the same solar wind conditions as listed in Table 1, but instead of an exosphere, a perfectly conducting Ceres is used for the inner boundary condition. The real brine conductivity is smaller than this perfect conducting case that we use, so the shock would be even smaller than that of our case 5 result. Figure 6 shows our case 5 model result in 2-D projections. The flaring angle of the shock is smaller than that of the mass loading shocks, so the same set of IMF field lines used to illustrate the tangency at the shock surface can no longer touch the shock. However, we believe a different IMF cone angle with a stronger B_x component, although less probable, could still touch the shock surface and cause fast-Fermi acceleration.

We note that the shock appears to have lasted for a week, which would require a large, comparably long-lived magnetic cloud to be present. The hypothesis presented by *Russell et al.* [2016] was that a magnetic cloud magnetized an imperfectly conducting Ceres, and the induced magnetization on the Ceres interior increased and then decreased. The problem with this scenario is that the conductivity of Ceres is expected to be too low and the duration of magnetization to be too short to mimic the observed 7 day events.

3.6. Case 6: The Gyroradius Effect

The gyroradius of water pickup ions is on the order of 50 R_c in the uncompressed solar wind. On the scale of our simulation domain, these water group ions move along the convection electric field, which should affect the shape of the shock. Asymmetry is expected because of the limited ion Larmor radius [*Hansen et al.*, 2007]. *Rubin et al.* [2014] have compared multifluid and hybrid models for a slightly smaller pickup rate (0.8×10^{26}/s) around a comet. Both models behave the same upstream, while the hybrid result shows striations downstream. Thus, our multifluid model provides a sufficient tool for estimating shock positions. Here in case 6p, we use the multifluid equations described in section 2.2, with parameters similar to those used in case 1, to show the effect of gyromotion.

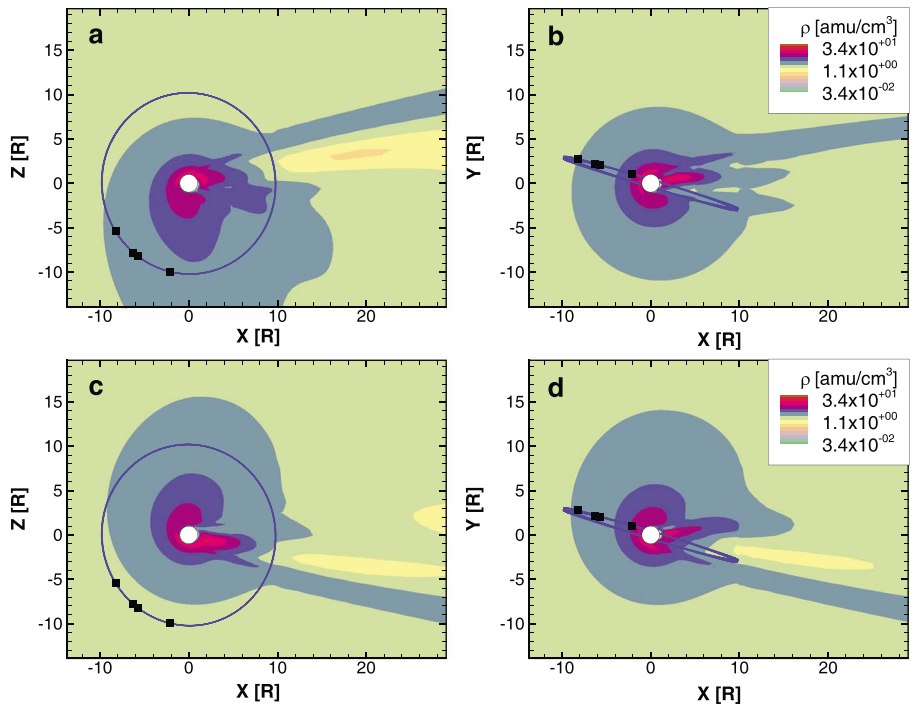

Figure 7. Case 6, Ceres shock produced by multifluid code. (a, b) A multifluid code running with parameters same as case 1, (c, d) the effect of reversing the sign of IMF used for the case shown in Figures 7a and 7b (Changing **B** to -**B**).

Figure 7 shows the density profile produced by the multifluid model in the *x*-*y* and *x*-*z* planes, which is significantly different from the single-fluid MHD model. The density contour shows total density increase in a much broader region, as represented by the outermost blue contour level ranging from −7 to 14 R_c on the upstream side of Ceres. This is because the water ions are no longer averaged into the protons as in the single-fluid code. However, the number density in this region is not significantly different from the single-fluid MHD result. We find that the proton density did not increase in this region, while water group number density is about 3% the proton number density (not plotted). This region is the local pickup region. The flow is not significantly slowed, as indicated by the proton density. Thus, the flow did not form a shock at this distance.

In Figures 7a and 7b, the blue contour line extends more on the −*z*/south side than on the +*z*/north side, because the convection electric field is pointing +*z*, accelerating the pickup ions. Accordingly, the density gradient to the south of Ceres is smaller than the gradient to the north of Ceres, making it hard to form a well-defined shock surface to the south of Ceres. The shock surface is only seen to the north of Ceres, represented by the innermost contour line (red color) in Figure 7. Upstream of the shock, about 24% of the total ions are water ions. Although the subsolar distance of the shock is at 1.5 R_c, which is farther out than that of the case 1 result, the flaring angle of the shock to the north of Ceres is smaller than that of the case 1 result.

Even though the IMF cone angle is constrained by the shock surface, the field can be either positive or negative. Reversing the IMF by 180° reverses the electric field that accelerates the pickup ions and thus flips the side of the shock that is pushed outward, as concluded in case 6n run shown in Figures 7c and 7d. As expected, Figures 7a and 7c are similar after either one is flipped by 180° about the Ceres-Sun line (the *x* axis). Comparing Figure 7a and 7c, we conclude that, to create a well-defined shock surface that accelerates electrons back toward Dawn, the magnetic field vector must point toward +*x* (from the Sun to Ceres) and −*y*. In the 7 day period, reversals in the polarity of the IMF are seen in the ACE data, indicating heliospheric current sheet (HCS) crossings. Such an IMF direction will not change the conclusions drawn from previous cases, cases 1–5, because these single-fluid runs are not affected by the limited gyroradius effect.

A weaker compression gradient indicates that the minimum outgassing rate of a global atmosphere should be larger than the 1.8 kg/s lower limit suggested by our single-fluid atmosphere model. Our parameter study

has found 3 kg/s to be an appropriate lower limit for such assumptions. However, if the outgassing is in a plume, as was shown in section 3.3, the outgassing rate can still be lower than 3 kg/s.

4. Discussion and Conclusions

In this study we treat the shock surface as a thin discontinuity, while in reality, the shock thickness may be more than tens of kilometers [*Schwartz et al.*, 2011]. Using the case 1 parameters, the proton and electron gyroradii are 2 R_c and 0.002 R_c, respectively. The proton and electron inertial lengths are 0.4 R_c and 0.01 R_c, respectively. Measured by these critical lengths, if the Ceres shock thickness is comparable to that of the Earth, our assumption is still applicable. Nevertheless, a hybrid model on the magnetic induction case [*Lindkvist et al.*, 2015] and on thin air interaction at Ceres [*Lindkvist et al.*, 2017] may improve the accuracy of such shock thickness estimations.

In section 3.6 we examined the density ratio between pickup ions and solar wind protons at the shock. A density increase upstream of a shock is typical for cometary pickup shocks. *Biermann et al.* [1967] calculated a critical limit for mass loading. The flow has to become shocked after the number density ratio of picked-up CO^+ ions to protons exceeds 2%. This was later found to be consistent with in situ observation at comets [i.e., *Wilken et al.*, 1987]. *Koenders et al.* [2013] examined this number with MHD and hybrid models but found other factors like the IMF cone angle and IMF strength to affect the shock distance as well. *Shou et al.* [2015] used a single-fluid, multispecies MHD model to find that the shock distance varies widely for comets at heliocentric distances 0.17 to 1.75 AU, in contrast to the Biermann model. In our case 1 model result, the shock formed along the comet-Sun line when the number density ratio between pickup ions and total ions was about 10%, while our case 6 result increased to 24%. We believe this is due to the significant decoupling between pickup ions and protons, or the limited gyroradius effect for such weak pickup interactions: the gas production ratio is 3 orders of magnitude smaller than that of comet 1P/Halley. Shock formation itself is not the goal of this paper, but the transition between shock formation and a kinetic pickup wake has been studied extensively recently, using both modeling [*Rubin et al.*, 2015] and Rosetta observations, when comet 67P/Churyumov–Gerasimenko was at 3.4 AU with an outgassing rate of about 5×10^{25}/s [*Broiles et al.*, 2015]. This Ceres study may add more knowledge to this transition problem.

Dissociative recombination [*Jia et al.*, 2007] is neglected in both models that we used. At the shock, the rate of recombination reactions is about 5 orders of magnitude smaller than the charge exchange reaction rate, because the electron density is orders of magnitude lower than the neutral density. Their importance may increase in the tail where neutral density drops [*Shou et al.*, 2015], but we can safely neglect them for our shock location estimation.

Elastic collisions between ions, neutrals, and electrons [*Ofman*, 2004; *Rubin et al.*, 2014] are not explicitly included in our equations, but their effects are adopted into some inelastic collision terms, where neutral t and neutral s' are the same species. Nevertheless, the ion-electron collision is not included in such combinations. In addition, the coefficient of elastic collision is slightly smaller than that of the charge exchange rate for the water group ions [*Shou et al.*, 2015]. With the set of reaction rates we used, the effect of the charge exchange rate becomes comparable with the impact ionization rate only when the plasma number density goes higher than 5/cm^3, while the plasma density is below 5/cm^3 in most of our calculation domain.

The escape velocity on Ceres surface is about 500 m/s, while the thermal velocity of 180 K water vapor is only 300 m/s. The gas may be more concentrated on the surface than the exosphere model used. Comparable to the plume results studied in the case 3 runs, a higher concentration of water vapor causes stronger shocks, allowing the lower limit of the total production rate to be below the 6×10^{25}/s value. On the other hand, the upper limit of this outgassing rate set by previous observations is sufficient to create a shock, if the IMF is in the preferred direction.

In Figures 1 and 2, we used the same IMF to connect all four events to the shock surface. In reality, the IMF can be different at the four time intervals of detection. However, our multifluid model requires the IMF to point antisunward. We used case 4 to discuss the effect of solar wind. It is possible that the ionization rate is higher than what we used, due to impact ionization and solar activities. In that case, the shock can be stronger, and the lower limit of the outgassing rate can be even lower than 1.8 kg/s.

In our model, the electron temperature is calculated arbitrarily from the ion temperature [*Gombosi et al.*, 1996]. It is possible that the electron temperatures can be different from proton temperatures upstream. In addition,

an electron energy equation should be solved to strictly describe the pressure contribution from the electrons. In our shock location estimate, in which the dynamic pressure is balanced by magnetic pressure, we do not expect a change in the electron temperature to have any significant effect on our conclusion.

As discussed in sections 2 and 3, there are simplifications in our model: uncertainties and time variability in the upstream solar wind conditions, electron temperature isotropy, ion gyroradius effect on the downstream, reaction in the wake, detailed chemical reactions involving more species, changes in surface temperature [*Formisano et al.*, 2016], waves, and surface conductivity. Nevertheless, our model catches the major interaction processes to estimate the range of the total production rate.

We do show the effect of asymmetric exosphere and brine conductivity. Plumes produce stronger shocks for an equivalent gas loss rate as a global exosphere, but the asymmetric shape of the shock created by a plume should be rhythmically moving in and out, as modulated by both the source corotation and solar wind variation.

Similarly, the bow shock shape created by a conductive layer beneath the surface is too narrow to have reasonable IMF directions tangent to the shock surface and does not persist long enough to be consistent with Dawn measurements. For these reasons, we favor a global exosphere as the source for producing a temporary bow shock. A rough estimation for the possible outgassing rate is between 3×10^{26}/s, or 9 kg/s, and 6×10^{25}/s, or 1.8 kg/s. This result is consistent with the outgassing rates observed by *A'Hearn and Feldman* [1992], *Küppers et al.* [2014], and *Roth et al.* [2016] and allows for IMF directions tangent to the shock that are consistent with the ACE data extrapolation.

Acknowledgments
This work is supported by NASA contract NNM05AA86C to the University of California, Los Angeles. The simulations are performed on Pleiades, provided by the NASA High-End Computing (HEC) Program through the NASA Advanced Supercomputing (NAS) Division at Ames Research Center. The solar wind data used can be found following the link provided in section 2.3. Dawn GRaND data are available on PDS.

References

A'Hearn, M. F., and P. D. Feldman (1992), Water vaporization on Ceres, *Icarus*, *98*, 54–60, doi:10.1016/0019-1035(92)90206-M.

Biermann, L., B. Brosowski, and H. U. Schmidt (1967), The interactions of the solar wind with a comet, *Sol. Phys.*, *1*, 254–284.

Broiles, T. W., J. L. Burch, G. Clark, C. Koenders, E. Behar, R. Goldstein, S. A. Fuselier, K. E. Mandt, P. Mokashi, and M. Samara (2015), Rosetta observations of solar wind interaction with the comet 67P/Churyumov-Gerasimenko, *Astron. Astrophys.*, *583*, A21, doi:10.1051/0004-6361/201526046.

Castillo-Rogez, J. C. (2011), Ceres—Neither a porous nor salty ball, *Icarus*, *215*, 599–602, doi:10.1016/j.icarus.2011.08.007.

Formisano, M., M. C. De Sanctis, G. Magni, C. Federico, and M. T. Capria (2016), Ceres water regime: Surface temperature, water sublimation and transient exo(atmo)sphere, *Mon. Not. R. Astron. Soc.*, *455*, 1892–1904, doi:10.1093/mnras/stv2344.

Gombosi, T. I., D. L. De Zeeuw, R. M. Häberli, and K. G. Powell (1996), Three-dimensional multiscale MHD model of cometary plasma environments, *J. Geophys. Res.*, *101*, 15,233–15,252, doi:10.1029/96JA01075.

Hansen, K. C., T. Bagdonat, U. Motschmann, C. Alexander, M. R. Combi, T. E. Cravens, T. I. Gombosi, Y.-D. Jia, and I. P. Robertson (2007), The plasma environment of comet 67P/Churyumov-Gerasimenko throughout the rosetta main mission, *Space Sci. Rev.*, *128*(1–4), 133–166, doi:10.1007/s11214-006-9142-6.

Jia, Y.-D., M. R. Combi, K. C. Hansen, and T. I. Gombosi (2007), A global model of cometary tail disconnection events triggered by solar wind magnetic variations, *J. Geophys. Res.*, *112*, A05223, doi:10.1029/2006JA012175.

Jia, Y. D., C. T. Russell, K. K. Khurana, G. Toth, J. S. Leisner, and T. I. Gombosi (2010), Interaction of Saturn's magnetosphere and its moons: 1. Interaction between corotating plasma and standard obstacles, *J. Geophys. Res.*, *115*, A04214, doi:10.1029/2009JA014630.

Jia, Y.-D., C. T. Russell, W. Liu, and Y. S. Shou (2014), Multi-fluid model of a Sun-grazing comet in the rapidly ionizing, magnetized low corona, *Astrophys. J.*, *796*, 42, doi:10.1088/0004-637X/796/1/42.

Koenders, C., K.-H. Glassmeier, I. Richter, U. Motschmann, and M. Rubin (2013), Revisiting cometary bow shock positions, *Planet. Space Sci.*, *87*, 85–95, doi:10.1016/j.pss.2013.08.009.

Küppers, M., et al. (2014), Localized sources of water vapour on the dwarf planet (1)Ceres, *Nature*, *505*, 525–527, doi:10.1038/nature12918.

Lindkvist, J., M. Holmström, K. K. Khurana, S. Fatemi, and S. Barabash (2015), Callisto plasma interactions: Hybrid modeling including induction by a subsurface ocean, *J. Geophys. Res. Space Physics*, *120*, 4877–4889, doi:10.1002/2015JA021212.

Lindkvist, J., M. Holmström, S. Fatemi, M. Wieser, and S. Barabash (2017), Ceres interaction with the solar wind, *Geophys. Res. Lett.*, *44*, 2070–2077, doi:10.1002/2016GL072375.

Ofman, L. (2004), Three-fluid model of the heating and acceleration of the fast solar wind, *J. Geophys. Res.*, *109*, A07102, doi:10.1029/2003JA010221.

Prettyman, T. H., et al. (2011), Dawn's gamma ray and neutron detector, *Space Sci. Rev.*, *163*, 371–459, doi:10.1007/s11214-011-9862-0.

Roth, L., N. Ivchenko, K. D. Retherford, N. J. Cunningham, P. D. Feldman, J. Saur, J. R. Spencer, and D. F. Strobel (2016), Constraints on an exosphere at Ceres from Hubble Space Telescope observations, *Geophys. Res. Lett.*, *43*, 2465–2472, doi:10.1002/2015GL067451.

Rubin, M., et al. (2014), Plasma environment of a weak comet—Predictions for Comet 67P/Churyumov-Gerasimenko from multifluid-MHD and Hybrid models, *Icarus*, *242*, 38–49, doi:10.1016/j.icarus.2014.07.021.

Rubin, M., T. I. Gombosi, K. C. Hansen, W.-H. Ip, M. D. Kartalev, C. Koenders, and G. Tóth (2015), Modeled interaction of comet 67P/Churyumov-Gerasimenko with the solar wind inside 2 AU, *Earth Moon Planets*, *116*, 141–157, doi:10.1007/s11038-015-9476-8.

Russell, C. T., et al. (2016), Dawn arrives at Ceres: Exploration of a small, volatile-rich world, *Science*, *353*, 1008–1010, doi:10.1126/science.aaf4219.

Schwartz, S. J., E. Henley, J. Mitchell, and V. Krasnoselskikh (2011), Electron temperature gradient scale at collisionless shocks, *Phys. Rev. Lett.*, *107*(21), 215002, doi:10.1103/PhysRevLett.107.215002.

Shou, Y., M. Combi, Y.-D. Jia, T. Gombosi, G. Toth, and M. Rubin (2015), The plasma environment in comets over a wide range of heliocentric distances: Application to comet C/2006 P1 (McNaught), *Astrophys. J.*, *809*, 156, doi:10.1088/0004-637X/809/2/156.

Smith, E. J., and J. H. Wolfe (1979), Fields and plasmas in the outer solar system, *Space Sci. Rev.*, *23*, 217–252, doi:10.1007/BF00173811.

Villarreal, M. N., C. T. Russell, J. G. Luhmann, W. T. Thompson, T. H. Prettyman, M. F. A'Hearn, M. Küppers, L. O'Rourke, and C. A. Raymond (2017), The dependence of the Cerean exosphere on solar energetic particle events, *Astrophys. J. Lett.*, *838*, L8, doi:10.3847/2041-8213/aa66cd.

Wilken, B., A. Johnstone, A. Coates, E. Amata, and H. Borg (1987), Pick-up ions at Comet P/Halley's bow shock—Observations with the IIS spectrometer on Giotto, *Astron. Astrophys.*, *187*, 153–159.

Wu, C. S. (1984), A fast Fermi process—Energetic electrons accelerated by a nearly perpendicular bow shock, *J. Geophys. Res.*, *89*, 8857–8862, doi:10.1029/JA089iA10p08857.

Zhang, H., et al. (2016), Alfvén wings in the lunar wake: The role of pressure gradients, *J. Geophys. Res. Space Physics*, *121*, 10,698–10,711, doi:10.1002/2016JA022360.